PHYSICAL REVIEW FLUIDS **2**, 014301 (2017)

Shearing flow from transient bubble oscillations in narrow gaps

Milad Mohammadzadeh, Fenfang Li, and Claus-Dieter Ohl[*]
Division of Physics and Applied Physics, School of Physical and Mathematical Sciences, Nanyang Technological University, 637371 Singapore

(Received 12 August 2016; published 23 January 2017)

The flow driven by a rapidly expanding and collapsing cavitation bubble in a narrow cylindrical gap is studied with the volume of fluid method. The simulations reveal a developing plug flow during the early expansion followed by flow reversal at later stages. An adverse pressure gradient leads to boundary layer separation and flow reversal, causing large shear stress near the boundaries. Analytical solution to a planar pulsating flow shows qualitative agreement with the CFD results. The shear stress close to boundaries has implications to deformable objects located near the bubble: Experiments reveal that thin, flat biological cells entrained in the boundary layer become stretched, while cells with a larger cross section are mainly transported with the flow.

DOI: 10.1103/PhysRevFluids.2.014301

I. INTRODUCTION

Strongly oscillating bubbles in narrow gaps are commonly found in microfluidic applications of cavitation. These bubbles can be generated with focused laser pulses [1–3], with acoustically excited capillary waves [4], or through spark discharges [5]. Applications of these transient pulsating flows span cell stretching [6,7], liquid pumping [8], switching and sorting [9,10], mixing [11], and droplet generation [12].

Modeling the fluid flow in these applications has been done to various degrees of sophistication. Over a sufficiently short time scale, the problem can be simplified as a planar inviscid flow leading to a Rayleigh-type equation in cylindrical coordinates [13]. This potential flow description has been extended to nonspherical bubbles in narrow gaps [14]. However, a notable deficiency of these approximations is their inability to model boundary layers, which are important when dealing with suspended objects near the walls, e.g., flat red blood cells and thin elastic objects such as nanowires [15]. Our recent experiments on bubble-induced cell stretching, such as red blood cells [7], gave motivation to model the fluid flow in order to understand the underlying flow patterns that causes cell deformation. In the present work, we focus on the structure of the liquid flow, i.e., the formation of boundary layers during the expansion and collapse cycle of a single transient bubble.

In general, this confined flow may be simplified to an axisymmetric radial flow forced by a time-dependent source at the origin. Axisymmetric radial flows in narrow gaps have been studied experimentally and analytically in the past fifty years due to their relevance in industrial applications such as radial viscometers, radial diffusers, nonrotating air bearings, and disk type heat exchangers. For an oscillating source between two parallel plates, in which the source strength varies sinusoidally about a zero-mean value, Elkouh [16] obtained an analytical solution and reported reversed flow near the walls. Zitouni and Vatistas [17] provide an analytical power series solution to purely accelerating and decelerating flows between two flat disks, which has later been studied numerically in Ref. [18] as well. Although the flow reversal is not captured with the solution provided in Ref. [17], it can be deduced to occur once the derivative of the velocity in the axial direction becomes zero at the wall. Von Kerczek [19] completed the work of Zitouni and Vatistas [17] by finding analytical solutions for the cases where flow reversal indeed happens, i.e., where the flow is neither purely accelerating nor decelerating.

---

[*] cdohl@ntu.edu.sg

Several groups have investigated bubble pulsations in a confinement. Cui *et al.* [20] studied analytically the response of an acoustically driven spherical bubble confined between two parallel plates. In this study, although the bubble is much smaller than the gap height, the channel walls affect the bubble dynamics. As the spherical bubble is confined between two plates, decreasing the channel height reduces the resonance frequency and the maximum response amplitude of the bubble. Large bubbles, in contrast, obtain a cylindrical shape bounded by the walls, which is referred to as a cylindrical bubble. Ilinskii *et al.* [21] obtained a solution for harmonic cylindrical bubble pulsations in an infinite domain of compressible liquid. They compared their model with the Gilmore equation for cylindrical bubble oscillations and also with the commonly used two-dimensional Rayleigh-Plesset equation, emphasizing the role of liquid compressibility.

Considering the application of microbubbles as a pumping mechanism, Ory *et al.* [22] have simulated the viscous flow induced by growth and collapse of a bubble in a narrow tube. In a similar geometry, a detailed study of the liquid flow field induced by bubble activity has been reported by Ye and Bull [23]. They have conducted direct numerical simulation of microbubble expansion and shrinkage in a long tube, which represents the bubble activity in human vascular system during gas embolotherapy. An improved model with flexible walls was presented in Ref. [24]. In another biomedical application of microbubble expansion, the deformation of cells has been modeled with a boundary element method by Tandiono *et al.* [25], which accounts for the membrane tension of the cell. Their finding is that deformation of a cell, modeled as a liquid droplet, is maximized if the resonance frequency of its surface mode matches the oscillation period of the bubble. This shape frequency is dependent on the density contrast of the liquids and the membrane tension. The model provides a physical explanation for why the shape of an elastic object in a symmetric back-and-forth motion does not return to its original state, in contrast to a fluid particle in a homogeneous flow. Yet, the no-slip boundaries were ignored by Tandiono *et al.* [25].

In the present work we focus on unsteady boundary layers generated in close proximity of an oscillating bubble between two parallel disks using numerical simulations of the flow. The rapidly expanding bubble is assumed to be created by an intense, focused laser pulse as a method of impulsive deposition of energy in the liquid. The simulation results are compared to an analytical expression for planar flow induced by an oscillating pressure gradient. A simple experiment using deformable biological cells of different sizes was conducted, where the cells probe the shear stress through their deformation.

II. NUMERICAL SIMULATION

A. Computational domain

The problem modeled is the expansion and shrinkage of an initially spherical bubble, created by a focused, high-power laser pulse. The bubble is located at the center and between two parallel discs separated by a gap of height $h = 20\ \mu\text{m}$. We assume axisymmetry and only model the upper quarter of the gap, utilizing symmetry to reduce the computational costs; see Fig. 1. The computational domain is drawn to scale, with the length being $\overline{\text{AB}} = 80\ \mu\text{m}$ and the height $h/2 = \overline{\text{DA}} = 10\ \mu\text{m}$.

The complex physical process of laser-matter interaction [26] leading to a rapidly expanding bubble is greatly simplified by starting the simulation with a bubble of finite size and filled with noncondensible gas; see Refs. [27] and [25]. The liquid motion around the bubble happens on a time scale of tens of microseconds, while the acoustic transients are significant for at most hundreds of nanoseconds [26,28]. Therefore, for the purpose of resolving the pressure and velocity field in the liquid surrounding the bubble, liquid compressibility effects and acoustic transients could be safely neglected.

B. Numerical solver specifications

The multiphase flow problem of the compressible gas and the incompressible liquid is modeled with the volume of fluid (VOF) method accounting for interfacial tension but neglecting body forces using ANSYS FLUENT 14.0 [29]. The boundary conditions as depicted in Fig. 1 are along $\overline{\text{DA}}$ axis of symmetry, between $\overline{\text{AB}}$ symmetry, at $\overline{\text{BC}}$ constant pressure p_0, and no slip at $\overline{\text{CD}}$. In the VOF

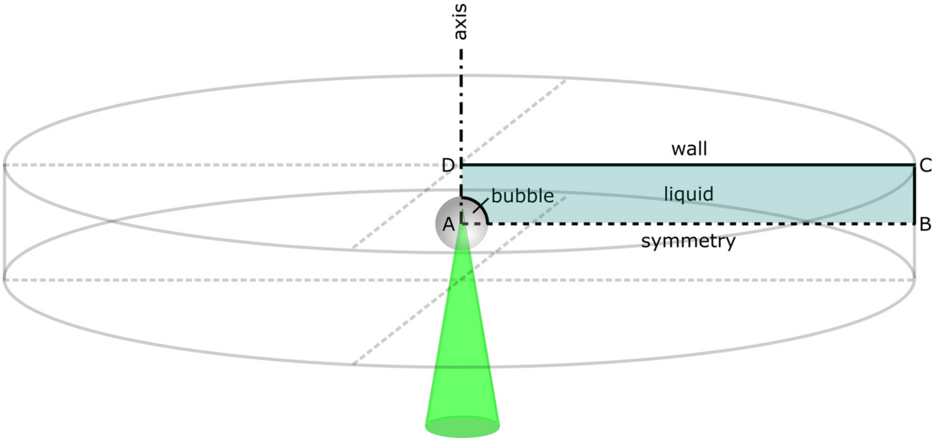

FIG. 1. Sketch of the computational domain using axisymmetry and symmetry with respect to the center plane of the gap.

method a single set of momentum equations is solved for all phases, meaning that the pressure and velocity field are shared among all present phases, and the volume fraction of each phase is tracked throughout the domain. The momentum equation is

$$\frac{\partial}{\partial t}(\rho\vec{v}) + \nabla\cdot(\rho\vec{v}\vec{v}) = -\nabla p + \nabla\cdot[\mu(\nabla\vec{v} + \nabla\vec{v}^T)] + \vec{F}, \tag{1}$$

where ρ is the density of the phases, $\vec{v}$ is the velocity, p is the pressure, and $\vec{F}$ is the surface force. The surface force is modeled as a continuum surface force (CSF) as proposed in Ref. [30]. In ANSYS FLUENT, the surface curvature is calculated from local gradients in the surface normal at the interface of phases. In solving the governing equations, the material properties, such as density, ρ, or viscosity, μ, are calculated as volume-fraction-averaged properties. Interface tracking is done by coupling the volume of fluid with the level-set method [31,32]. This allows for accurate interface tracking as well as mass conservation, in spite of the large density difference between the bubble content and the liquid.

In the present simulation, the pressure implicit with splitting of operators (PISO) scheme is used for pressure-velocity coupling. The pressure staggering option (PRESTO!) is chosen for the spatial discretization of the pressure while second-order upwind differencing is used in solving the governing equations. The geo-reconstruct method is implemented for discretization of volume fraction and interface reconstruction. An absolute convergence criteria of 10^{-6} is used for all governing equations and the time step in the simulation is 10^{-8}s . To assure the solution is mesh independent, the simulations were conducted with two different grids, 5 000 and 80 000 elements, with an averaged element size of 0.4 and 0.1 μm, respectively. Both solutions are nearly identical, see Fig. 3, and therefore grid independence is obtained. All results reported here are using 0.1-μm element size, while the mesh is refined in regions with high gradients, e.g., the initial bubble-liquid interface and near the channel walls. The simulation time on a 2.1-GHz Intel Core i7 personal computer with 8 GB of RAM is approximately 24 h for a single cycle of bubble expansion and shrinkage.

The initial pressure in the gas bubble of $R(t = 0) = 5\ \mu$m is 100 bar. The liquid is initially at atmospheric pressure $p_0 = 1$ bar. The liquid is water with a density of $\rho_l = 998.2\ \mathrm{kg/m^3}$ and a dynamic viscosity of $\mu_l = 1 \times 10^{-3}$ Pa s, while the gas viscosity is $\mu_b = 1.34 \times 10^{-5}$ Pa s, corresponding to water vapor. The ideal gas law is used for calculation of density of the compressible bubble content. This density calculation requires the solution to the energy equation [29], which is shared among both phases, similar to the momentum equation (1). The temperature field is initially assumed to be uniform in the computational domain and at 300 K. The interfacial tension coefficient is $\gamma = 7.2 \times 10^{-2}$ N/m.

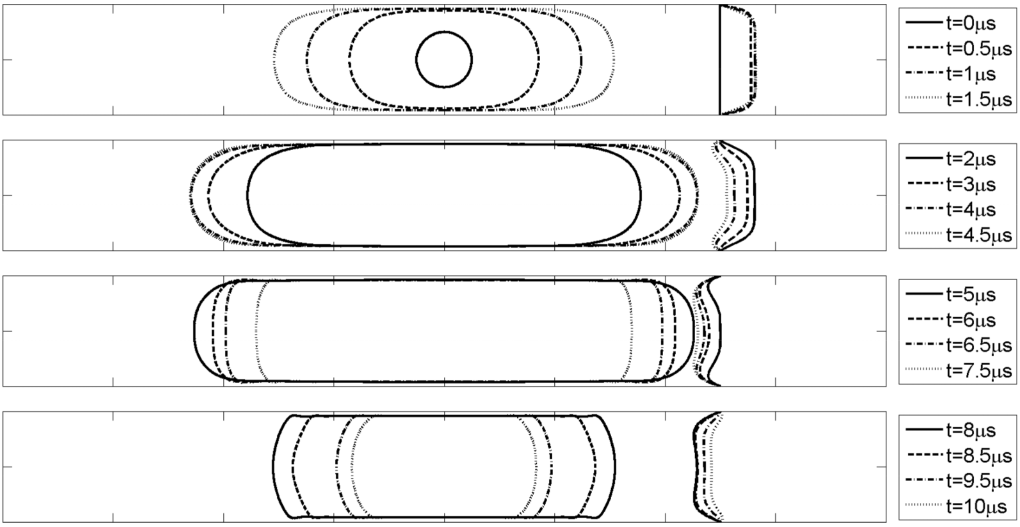

FIG. 2. Computational fluid dynamics (CFD) results of the bubble shape evolution together with the radial liquid velocity profile at $r = 50\,\mu$m from the center of the bubble. Please note the reversal of the flow direction near the boundaries occurring before the flow in the center of the gap.

III. CFD RESULTS AND ANALYSIS OF THE FLOW FIELD

A. Bubble evolution and liquid velocity profile

Figure 2 depicts the temporal evolution of the bubble shape over a period of 10 μs in a gap of $h = 20\,\mu$m. The spherical bubble quickly grows into a pancake shape, forming thin liquid films at the upper and lower solid walls. The maximum bubble radius is obtained after 4 μs. During bubble shrinkage, the convex interface flattens and only increases curvature after 8 μs, that is, when the internal pressure increases and dampens the collapse of the bubble. The bubble collapses to its minimum volume at 10 μs and rebounds afterwards (not shown here). To the right of the bubble profile in Fig. 2, the radial velocity profile at a distance of $r = 50\,\mu$m from the bubble center is shown. Initially, the liquid is at rest and rapidly develops into a plug flow with strong wall shear stress. Gradually, a more parabolic profile develops. At the later expansion stage, the velocity near the walls is reduced and even reversed in direction, while the liquid velocity in the center of the gap is still outwards and positive. This flow reversal near the boundaries will be discussed in detail in Sec. III B.

Figure 3 shows the projected bubble radius from Fig. 2 and compares it with the experimentally determined radii [2] and a two-dimensional Rayleigh-Plesset equation, e.g., see Ref. [13]. For the chosen initial conditions, i.e., radius $R(t = 0)$ and initial gas pressure, we find a good agreement between the VOF simulation and the experiment. In particular, the asymmetry of the bubble oscillation, having a faster expansion than the collapse, is captured in the VOF simulation. Interestingly, this asymmetry was attributed previously and in a different geometry to thermal effects [33]. We speculate that the faster expansion and slower collapses is caused by the asymmetry of the flow: During expansion a plug flow prevails which has a lower overall viscous pressure head. Later the boundary layers develop, retarding the flow and therefore lengthening the collapse.

The final stage of bubble collapse cannot be captured with the VOF model as it assumes that the liquid and bubble content are immiscible, while in experiments the laser-generated bubble mainly consists of condensable vapor. Our simulation predicts a milder collapse with re-expansion of the bubble; however, the experiments find a much smaller minimum bubble radius followed by fragmentation of the bubble.

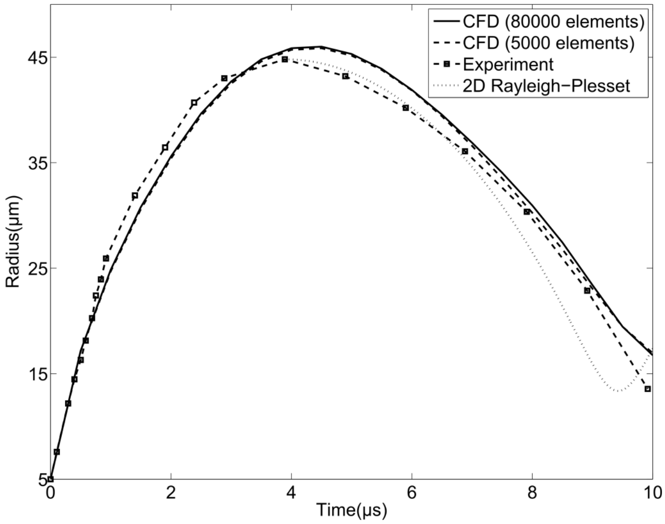

FIG. 3. Comparison of experimental cylindrical bubble dynamics [2] (dashed line with squares) with the VOF solution (filled line and dashed line for two computational grids). Additionally, the solution to the 2D Rayleigh-Plesset equation starting from the maximum bubble radius is shown with a dotted line.

B. Flow reversal due to adverse pressure gradient

For clarity we have divided the results into four stages and show the evolution of the liquid pressure, $p(r)$, and radial velocity $v_r(r = 50\,\mu\text{m}, z, t)$ in Fig. 4. The four stages from left to right are early expansion, late expansion, shrinkage, and rebound. The upper frames in Fig. 4 show the unsteady pressure in the center of the channel from $r = 0$ to the outlet, i.e., $p(r, z = 0, t)$. The axial pressure gradient is negligible in comparison to the significant pressure variation in the radial direction ($\partial p/\partial z \ll \partial p/\partial r$). Therefore, the pressure near the wall is nearly identical to the center; see also Fig. 6. The gas-liquid interface can be easily identified by the small pressure jump due to surface tension in the pressure profiles in Fig. 4. The lower frames of Fig. 4 show the velocity profile in the liquid at a fixed distance of $r = 50\ \mu\text{m}$ from the bubble center.

During the first stage, Fig. 4(a), $0 < t < 1.5\ \mu\text{s}$, the initial gas pressure of 100 bar accelerates the liquid outwards from rest to almost 7 m/s. In consequence, the gas pressure drops within 1.5 μs below the outlet pressure. During this time a flat-top velocity profile develops.

The second stage, Fig. 4(b), corresponds to the deceleration of the flow to the maximum bubble volume at $t = 4.3\ \mu\text{s}$. As the pressure in the bubble drops, an adverse pressure gradient develops ($\partial p/\partial r > 0$). This leads to detachment of the boundary layer, where a reversed flow at the boundary sets in. This flow reversal is clearly visible at $t = 4\ \mu\text{s}$ in the lower frame of Fig. 4(b). At this stage the flow profile possesses an inflection point; the liquid in the center of the channel continues to flow towards $+r$ while at the boundaries the flow is directed towards the bubble.

In the third stage, Fig. 4(c), the bubble shrinks; i.e., a net flow towards the bubble sets in and eventually a purely negative velocity profile builds up. In this stage the pressure gradient is stabilizing the boundary layer and the pressure in the bubble steadily builds up.

In the last stage, the bubble reaches its minimum volume and rebounds, Fig. 4(d), $8 < t < 10\mu s$. Similar to stage 1, the internal bubble pressure is higher than the liquid pressure, but here the liquid flow is toward the bubble. Therefore, the pressure gradient once again opposes the liquid flow and leads to flow reversal near the channel walls. The flow could be described similar to stage 2, but with opposite signs ($\partial p/\partial r < 0$). The liquid flow is eventually reversed at the walls in $t = 10\ \mu\text{s}$, minimum bubble volume is reached, and the bubble begins to rebound.

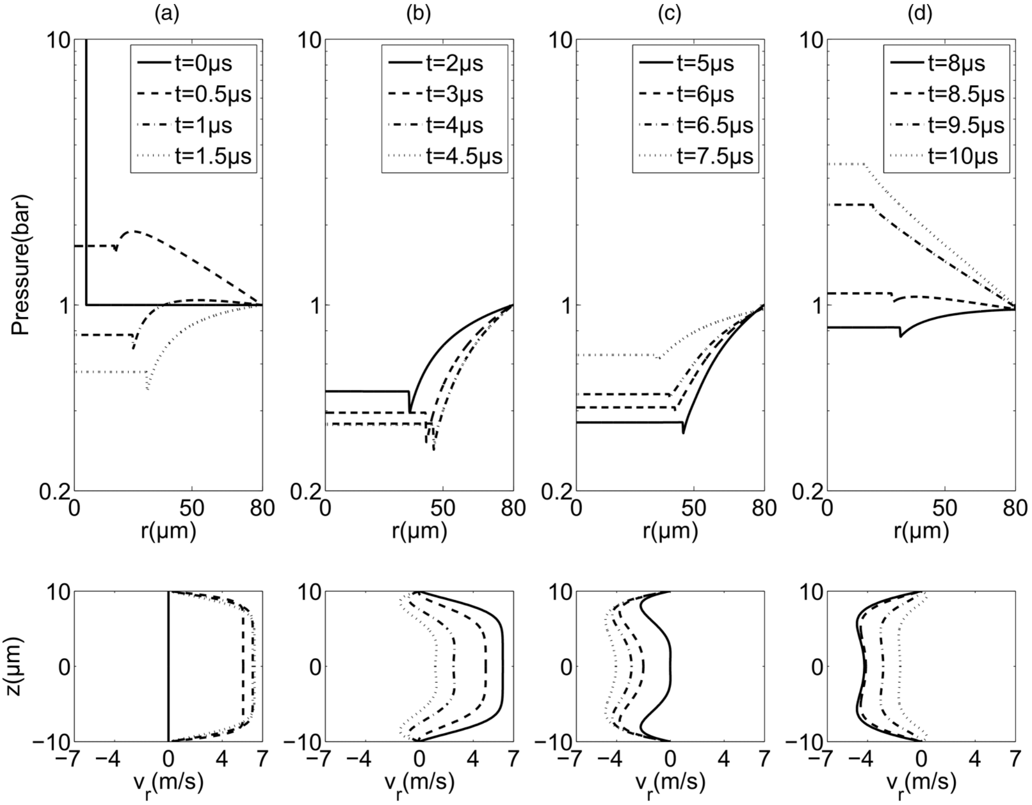

FIG. 4. Evolution of pressure (top row) and radial velocity (bottom row) during early (a) and late (b) expansion and early (c) and late (d) collapse. The times for the pressure and velocity profiles are indicated in the upper legend of each column.

C. Vorticity generation

Figure 5 depicts the instantaneous streamlines during the buildup and decay of the adverse pressure gradient together with a radial velocity profile at $r = 50\ \mu$m, corresponding to the late stage of bubble expansion in Fig. 4(b). At time $t = 3.5\ \mu$s formation of vortices near the channel walls is observed. From $t = 3$ to $4.5\ \mu$s the adverse pressure gradient supports the detachment of the boundary layer, leading to a recirculating flow. Due to symmetry two vortex rings are formed which are transported towards the center of the channel. In Fig. 5 the horizontal distance between the vortex core and the bubble wall remains approximately constant at about $5\ \mu$m. Additionally, the separation point of the boundary layer is relatively stable in space, here around $r = 44\ \mu$m, and only moves toward the bubble in the last frame of Fig. 5, i.e., at $t = 5.5\ \mu$s when the bubble gains inward speed. As both vortex rings migrate towards the center of the channel they merge, see Fig. 5, $t = 5.0$ and $5.5\ \mu$s. From then on, the radial flow and the pressure gradient are aligned, stabilizing the boundary layer.

D. Flow field contours

For clarity, we present a sequence of contour plots of the liquid flow during the bubble expansion and shrinkage in Fig. 6, in particular the pressure $p(r,z,t)$, the radial velocity $v_r(r,z,t)$, and the vorticity magnitude $|\nabla \times \vec{v}|$. The flow is separated into the same stages from Sec. III B.

At the early expansion of the bubble, ($t = 0.5\ \mu$s) in Fig. 6, the high pressure in the bubble accelerates the liquid outwards with a flat top radial velocity distribution with no vorticity in the central flow but shear and vorticity in the proximity of channel walls.

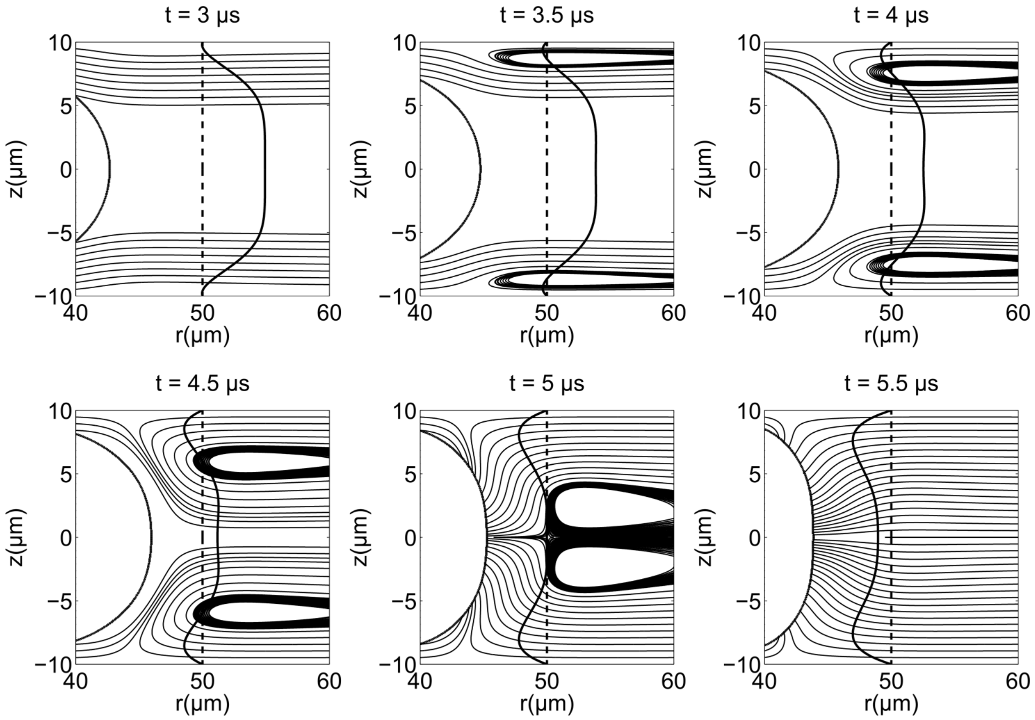

FIG. 5. Plot of the liquid streamlines during boundary layer separation, i.e., from $t = 3$ to 5.5 μs. The radial velocity profile is plotted at $r = 50$ μm. Two counter rotating vortices form, move upwards, and recombine.

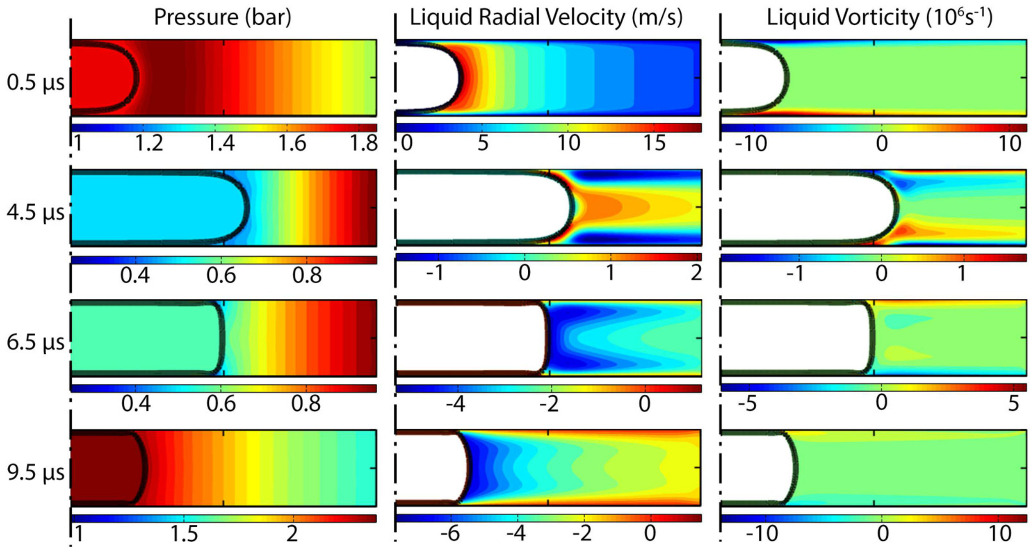

FIG. 6. Sequence of contour plots of the flow field during bubble expansion and shrinkage. Pressure field in both phases, radial velocity in the liquid, and vorticity in the liquid are shown at left, center, and right, respectively. The bubble-liquid interface is shown by the black line, i.e., contour of 0.5 liquid volume fraction. The color bar for each figure is given underneath. Each figure is plotted with its specific color map to better distinguish the flow field. Results are shown for a sample time instant of each different stage of the flow.

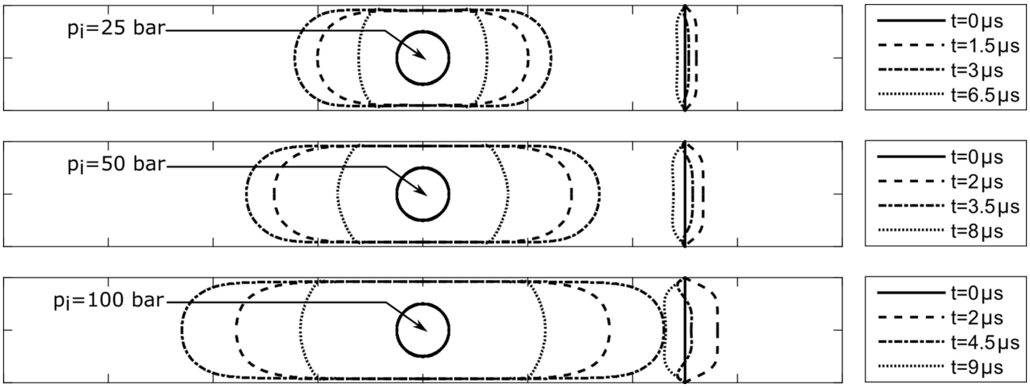

FIG. 7. The effect of initial internal bubble pressure p_i. Increasing the initial pressure results in a faster flow field and a larger bubble size, but important features such as flow reversal and vorticity generation are preserved. All simulations are done with $h = 20\ \mu$m and $\nu = 1$ cSt.

The late expansion and early shrinkage stage of the bubble ($t = 4.5\ \mu$s) is accompanied by the presence of reversed flow and boundary layer separation due to adverse pressure gradient in the liquid. The outward flow is stopped and reversed close to the walls and two counter rotating vortices are observed. The reversed flow and flow circulation in this stage cause significant shear stress near the walls.

As the inward flow sets in during the shrinkage ($t = 6.5\ \mu$s), the two vortices migrate toward the channel center until they eventually merge and circulation is not visible in the flow field anymore. The liquid flow toward the bubble is not opposed but stabilized by the pressure gradient.

Finally, the shrinkage causes the pressure to build up in the bubble ($t = 9.5\ \mu$s), which in turn acts as an adverse pressure gradient, opposing the inward liquid flow, and the bubble rebounds afterwards.

It is worth recalling that the solution to the Navier-Stokes equations using the volume of fluid method is shared among all phases, i.e., the water vapor in the bubble and its surrounding liquid water. This means that all variables, including the pressure and velocity, are obtained for both phases. In this paper, however, we focus only on the liquid flow field induced by the shared pressure field. Therefore, in Fig. 6, the radial velocity field and the vorticity field are shown only in the liquid.

E. Effects of initial pressure, channel height, and viscosity

We now study the importance of the initial gas pressure, the gap height, and the viscosity of the liquid independently. In Fig. 7 the temporal evolution of the bubble shape and the radial velocity at $r = 50\ \mu$m are compared for increasing internal bubble pressure from $p_i = 25$ to 100 bar. The channel height $h = 20\ \mu$m, the initial bubble size of $5\ \mu$m, and the liquid viscosity of 1 cSt are kept constant. By increasing the potential energy through internal pressure, the liquid is accelerated to a higher kinetic energy. The general features of the flow are observed across the tested pressure range, i.e., flow reversal and formation of vortices.

By increasing only the channel height, shown in Fig. 8, the bubble extends less in the radial direction. Meanwhile, it is observed that reversed flow and vorticity generation occur as long as the bubble covers the gap height. We can conclude that these flow features robustly occur for sufficiently large and rapidly expanding bubbles, regardless of the channel height.

As shown in Fig. 9, increasing the viscosity reduces the expansion velocity and thus the radial velocity gradient outside the boundary layer. Assuming a stationary outward flow with velocity U at the top of the boundary layer, we can relate the pressure gradient to the outward velocity as $\rho U dU/dr = -dp/dr$ based on the Bernoulli equation. Knowing that increasing the liquid viscosity reduces the outward flow velocity U and its radial gradient dU/dr, we can conclude

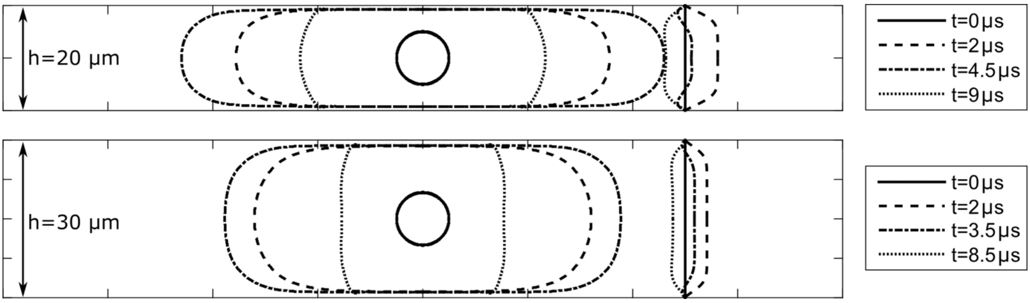

FIG. 8. Varying the channel height h from 20 to 30 μm. Flow reversal and vorticity generation near the walls are observed for a cylindrical bubble despite the gap height, but are more prominent in tighter confinements. Both simulations are done with $p_i = 100$ bar and $\nu = 1$ cSt.

that the pressure gradient also decreases at a higher viscosity. Since the pressure gradient is the driving force for separation, flow reversal is expected to be delayed or hindered at a higher viscosity. Figure 9 supports this idea: With increasing liquid viscosity the overall velocity is reduced. While flow reversal is still observed at the late expansion stage, it is less prominent in a more viscous liquid. Additionally, we observe that increasing the viscosity thickens the liquid film that separates the bubble from the channel walls.

IV. ANALYTICAL APPROXIMATION FOR LIQUID VELOCITY PROFILE: PULSATING PRESSURE-DRIVEN FLOW

The CFD solution reveals a complex flow pattern, yet we speculate that the main characteristics of the flow can be captured with fundamental solutions of unsteady flows. In the early stage of bubble expansion, the liquid in the channel is accelerated from rest to a velocity profile qualitatively similar to a Poiseuille flow. This acceleration of the liquid is accompanied by a rapid reduction in pressure inside the bubble.

Except for the short initial period described above, the pressure gradient acting on the liquid has a pulsating behavior for the majority of the bubble expansion and shrinkage cycle. At the onset of bubble shrinkage, the outlet pressure is higher than the pressure inside the bubble. Therefore, the flow near the boundaries is opposed by an adverse pressure gradient and is eventually reversed. As

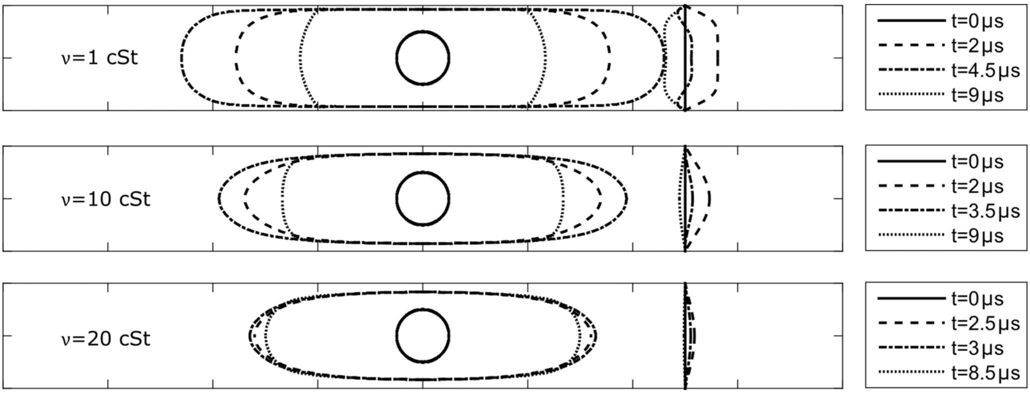

FIG. 9. The effect of kinematic viscosity ν: increasing the liquid viscosity while keeping $p_i = 100$ bar and $h = 20$ μm constant slows down the flow field considerably. The film thickness separating the bubble and channel walls is larger in a more viscous liquid.

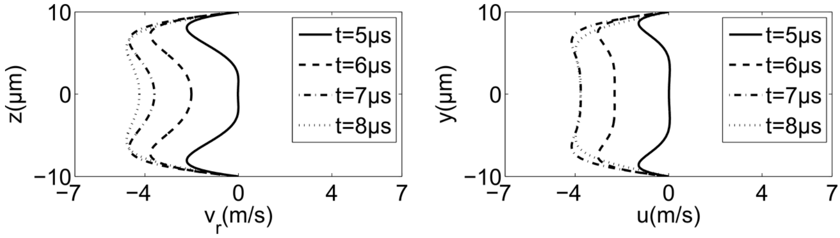

FIG. 10. Comparison of (left) the VOF simulation of the radial velocity with (right) the analytical approximation of the planar velocity profile during bubble shrinkage (2).

the inward flow sets in, the bubble shrinkage results in an increase in density and pressure of the gas, which in turn leads to opposition against the inward flow. This situation resembles an oscillating pressure gradient acting on the liquid between two parallel plates. Here we compare the simulation results with an analytical solution for a two-dimensional flow within a gap induced by an oscillating pressure gradient. Although the numerical solution is obtained for an axisymmetric geometry, we simplify the geometry to a planar flow in order to obtain an analytical solution.

Using a harmonic function for the pressure gradient, i.e., $\partial p/\partial x = \Delta p/\Delta x\ \sin\omega t$, we obtain the transient solution to the two-dimensional Navier-Stokes equation for incompressible flow between two parallel plates. To be succinct, we do not repeat the steps here and refer the reader to Sec. 7.8.3 of Ref. [34] for details of obtaining the analytical solution. The transient velocity profile $u(y,t)$ induced by this pulsating pressure-driven flow can be expressed as

$$u(y,t) = \frac{-1}{\rho\omega}\frac{\Delta p}{\Delta x}[f_c(y)\cos\omega t + f_s(y)\sin\omega t], \tag{2}$$

where $f(y)$ is given as a complex function with real and imaginary parts, $f_c(y)$ and $f_s(y)$, respectively. The complex function $f(y)$ is formulated as

$$f(y) = f_c(y) + i f_s(y) = 1 - \frac{\cosh\left(\left(\frac{2y}{h} - 1\right)\frac{h}{2}\sqrt{\frac{-i\omega\rho}{\mu}}\right)}{\cosh\left(\frac{h}{2}\sqrt{\frac{-i\omega\rho}{\mu}}\right)}\quad. \tag{3}$$

The pulsating velocity profile for the bubble shrinkage is approximated with the solution from (2) and is compared with the CFD solution in Fig. 10. A value of $\Delta p/\Delta x = 2.5\times\ 10^4$ bar m^{-1} with a period of $2\pi/\omega = 10\ \mu$s is used for the harmonic pressure gradient. This simplified analytical description is able to capture the general features of the bubble-driven flow during bubble shrinkage. Development of a reversed flow near the channel walls is observed, which later reverts completely toward the bubble. Later on, the pulsating pressure gradient opposes and decelerates the inward flow, which is similar to the findings in the numerical solution.

V. EXPERIMENTS: DEFORMATION OF CELLS

The numerical simulation suggests that deformable objects located within the boundary layer and close to the bubble may be stretched considerably by the shearing flow. We test this hypothesis with deformable objects thin enough to be entrained in the boundary layer, and larger objects which cover most of the channel. As deformable objects we use biological cells in a suitable aqueous solution (saline buffer solution). The experiments were stimulated from previous work with red blood cells [6,7]. Red blood cells are thin, biconcave cells with a diameter of about 8 μm and a thickness of less than 2 μm. After they are placed in the microfluidic gap, they sediment to the bottom because of their higher density. Figure 11(a) shows a typical configuration of red blood cells (RBCs) shortly before (top) and after (bottom) the bubble oscillation, as viewed from the top. RBCs near the bubble are largely stretched. We refer the reader to the Supplemental Material [35]

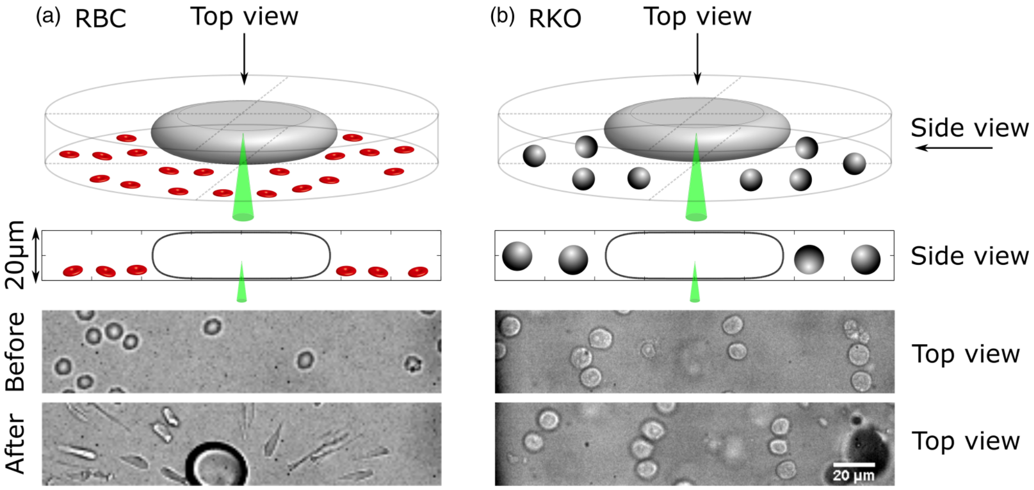

FIG. 11. Deformation of two different cell types due to the cavitation bubble induced flow in a 20-μm thin gap. (a) The top shows red blood cells (RBCs) just before a laser creates a single cavitation bubble and at the bottom are the cells just after the bubble collapse. (b) Colon cancer cells (RKOs) exposed to a similar flow before and after the cavitation bubble dynamics. RKOs are much less deformed compared to RBCs (see text).

for a sequence of photos depicting cell deformation in the experiments, which confirms that cell stretching occurs during late expansion and early shrinkage of the bubble. Details of the experiment are available in Refs. [6,7].

The simulations show that the boundary layer where stretching may occur is approximately 1 μm thick, which fits well with the thickness of red blood cells. Yet one would expect that cells covering a large part of the gap would behave differently. This is tested in a second experiment: Here we insert colon cancer cells (RKO), see Fig. 11(b), which have spherical shapes with a diameter of 10 to 15 μm, comparable with the 20-μm gap height. Figure 11(b) reveals that the RKO cells are transported with the flow but do not visibly stretch.

As the thin RBCs are comparable to the size of the vortex, they become exposed to a shearing force near the wall. From the simulation results, neglecting the presence of cells, we obtain values of about 2×10^6 1/s for the magnitude of the shear strain rate, $1/2(\partial v_r/\partial z + \partial v_z/\partial r)$, near the walls, where the RBCs are located. This can be related to a stretching of a fluid particle assuming a characteristic height and duration. Using 2 μm and a duration of 2 μs we obtain a length increase of 8 μm, a value which is of the order of the observed stretching in experiments, e.g., Ref. [7].

To the contrary, the spherical RKO cells extending into the center of the channel are advected with the flow. The shear stresses outside the boundary layer are considerably lower and therefore lead to weaker deformation. We find about 10% strain at the center of the channel over a thickness of 1 μm. The resulting deformation of these cells may be well within the resolution limit of the imaging optics.

VI. DISCUSSION AND CONCLUSION

A notable feature of the present numerical solution to the flow induced by a cavitation bubble in a narrow gap is the presence of boundary layer separation, reversed flow, and recirculation. In similar geometries, flow reversal has been reported by other investigators. In the case of *steady*, radial flow between two flat disks, extension of Von Kerczek [19] on the power-series solution obtained in Ref. [17] shows the existence of boundary layer separation in radial diffusers. Prior to that, flow visualization done in Ref. [36] on radial flows with a steady influx showed the nucleation, growth, migration, and eventual decay of vortices in the outward flow. Mochizuki and Yang [36] also obtained finite-difference solutions to the unsteady vorticity transport equation which were in agreement with their experimental findings. In an analytical treatment of the unsteady axisymmetric flow between two flat disks, Elkouh [16] found the radial velocity distribution induced by an oscillating source-sink exhibits flow reversal near the walls.

In a different confining geometry, an expanding bubble in a tube, direct numerical simulation of the flow reveals the presence of a recirculation region between the wall and the core flow at the end of bubble growth and beginning of shrinkage [23]. However, Ye and Bull [23] do not discuss this flow feature in greater depth, and instead focus on the wall pressure and shear stress which is aligned with the main application of their study, gas embolotherapy. Our findings about the wall shear stress due to bubble induced liquid flow in a microfluidic geometry agrees well with their report; thus, we refer the reader to Ref. [23] for a detailed discussion about wall shear stress. Interestingly, even inviscid boundary layer simulations may explain the deformation of dispersed droplets (being a simple model for a cell) if their interfacial tension is accounted for; see Ref. [25]. Tandiono *et al.* [25] simulated a droplet at some distance from an oscillating bubble in an infinite liquid. The interfacial tension introduces a second time scale besides the period of bubble oscillation; i.e., it causes the droplet to oscillate in a surface mode.

Utilizing a viscous model in the present study, we find that during the late expansion of a cavitation bubble in a narrow axisymmetric gap, the adverse pressure gradient leads to boundary layer separation and flow reversal in the proximity of the walls. Although such complex flow patterns in axisymmetry require computational treatment of the problem, a simplified analytical expression for planar pulsating flow supports our understanding of the series of events we observe in the numerical simulations and experiments. A prominent result of the observed flow reversal and vorticity is generation of strong shear stress in the liquid close to the boundaries. The results indicate that some flows created by oscillating bubbles in narrow gaps may not be accurately described with inviscid potential flow in cylindrical symmetry. Particularly, in studying the mixing and emulsification of flows or the deformation of elastic objects, such as yeast cells [37], it is necessary to account for the vorticity generation and transport. For both applications, it would be interesting to extend the present simulation to two-way coupling.

---

[1] Y.-H. Chen, H.-Y. Chu, and I. Lin, Interaction and Fragmentation of Pulsed Laser Induced Microbubbles in a Narrow Gap, Phys. Rev. Lett. **96**, 034505 (2006).

[2] E. Zwaan, S. Le Gac, K. Tsuji, and C.-D. Ohl, Controlled Cavitation in Microfluidic Systems, Phys. Rev. Lett. **98**, 254501 (2007).

[3] P. A. Quinto-Su, H.-H. Lai, H. H. Yoon, C. E. Sims, N. L. Allbritton, and V. Venugopalan, Examination of laser microbeam cell lysis in a PDMS microfluidic channel using time-resolved imaging, Lab Chip **8**, 408 (2008).

[4] Tandiono, S.-W. Ohl, D. S.-W. Ow, E. Klaseboer, V. V. T. Wong, A. Camattari, and C.-D. Ohl, Creation of cavitation activity in a microfluidic device through acoustically driven capillary waves, Lab Chip **10**, 1848 (2010).

[5] F. Ibn Azam, B. Karri, S.-W. Ohl, E. Klaseboer, and B. Cheong Khoo, Dynamics of an oscillating bubble in a narrow gap, Phys. Rev. E **88**, 043006 (2013).

[6] P. A. Quinto-Su, C. Kuss, P. R. Preiser, and C.-D. Ohl, Red blood cell rheology using single controlled laser-induced cavitation bubbles, Lab Chip **11**, 672 (2011).

[7] F. Li, C. U. Chan, and C. D. Ohl, Yield strength of human erythrocyte membranes to impulsive stretching, Biophys. J. **105**, 872 (2013).

[8] R. Dijkink and C.-D. Ohl, Laser-induced cavitation based micropump, Lab Chip **8**, 1676 (2008).

[9] T.-H. Wu, L. Gao, Y. Chen, K. Wei, and P.-Y. Chiou, Pulsed laser triggered high speed microfluidic switch, Appl. Phys. Lett. **93**, 144102 (2008).

[10] T.-H. Wu, Y. Chen, S.-Y. Park, J. Hong, T. Teslaa, J. F. Zhong, D. Di Carlo, M. A. Teitell, and P.-Y. Chiou, Pulsed laser triggered high speed microfluidic fluorescence activated cell sorter, Lab Chip **12**, 1378 (2012).

[11] A. N. Hellman, K. R. Rau, H. H. Yoon, S. Bae, J. F. Palmer, K. Scott Phillips, N. L. Allbritton, and V. Venugopalan, Laser-induced mixing in microfluidic channels, Anal. Chem. **79**, 4484 (2007).

[12] S.-Y. Park, T.-H. Wu, Y. Chen, M. A. Teitell, and P.-Y. Chiou, High-speed droplet generation on demand driven by pulse laser-induced cavitation, Lab Chip **11**, 1010 (2011).

[13] P. A. Quinto-Su and C.-D. Ohl, Interaction between two laser-induced cavitation bubbles in a quasi-two-dimensional geometry, J. Fluid Mech. **633**, 425 (2009).

[14] K. Y. Lim, P. A. Quinto-Su, E. Klaseboer, B. C. Khoo, V. Venugopalan, and C.-D. Ohl, Nonspherical laser-induced cavitation bubbles, Phys. Rev. E **81**, 016308 (2010).

[15] P. A. Quinto-Su, X. H. Huang, S. R. Gonzalez-Avila, T. Wu, and C. D. Ohl, Manipulation and Microrheology of Carbon Nanotubes with Laser-Induced Cavitation Bubbles, Phys. Rev. Lett. **104**, 014501 (2010).

[16] A. F. Elkouh, Oscillating radial flow between parallel plates, Appl. Sci. Res. **30**, 401 (1975).

[17] G. Zitouni and G. H. Vatistas, Purely accelerating and decelerating flows within two flat disks, Acta Mech. **123**, 151 (1997).

[18] W. S. Ghaly and G. H. Vatistas, Numerical computations of purely radial flow within two concentric disks, AIAA J. **39**, 1208 (2001).

[19] C. H. Von Kerczek, A note about the radial diffuser, Acta Mech. **135**, 229 (1999).

[20] J. Cui, M. F. Hamilton, P. S. Wilson, and E. A. Zabolotskaya, Bubble pulsations between parallel plates, J. Acoust. Soc. Am. **119**, 2067 (2006).

[21] Y. A. Ilinskii, E. A. Zabolotskaya, T. A. Hay, and M. F. Hamilton, Models of cylindrical bubble pulsation, J. Acoust. Soc. Am. **132**, 1346 (2012).

[22] E. Ory, H. Yuan, A. Prosperetti, S. Popinet, and S. Zaleski, Growth and collapse of a vapor bubble in a narrow tube, Phys. Fluids **12**, 1268 (2000).

[23] T. Ye and J. L. Bull, Direct numerical simulations of micro-bubble expansion in gas embolotherapy, J. Biomech. Eng.-T. ASME **126**, 745 (2004).

[24] T. Ye and J. L. Bull, Microbubble expansion in a flexible tube, J. Biomech. Eng. **128**, 554 (2006).

[25] T. Tandiono, E. Klaseboer, S.-W. Ohl, D. S.-W. Ow, A. B.-H. Choo, F. Li, and C.-D. Ohl, Resonant stretching of cells and other elastic objects from transient cavitation, Soft Matter **9**, 8687 (2013).

[26] W. Lauterborn and A. Vogel, Shock wave emission by laser generated bubbles, in *Bubble Dynamics and Shock Waves* (Springer, Berlin, 2013), pp. 67–103.

[27] S. R. Gonzalez-Avila, E. Klaseboer, B. C. Khoo, and C.-D. Ohl, Cavitation bubble dynamics in a liquid gap of variable height, J. Fluid Mech. **682**, 241 (2011).

[28] A. Vogel, S. Busch, and U. Parlitz, Shock wave emission and cavitation bubble generation by picosecond and nanosecond optical breakdown in water, J. Acoust. Soc. Am. **100**, 148 (1996).

[29] FLUENT ANSYS, 14.0 theory guide, ANSYS Inc. (2011).

[30] J. U. Brackbill, D. B. Kothe, and C. Zemach, A continuum method for modeling surface tension, J. Comput. Phys. **100**, 335 (1992).

[31] S. Osher and J. A. Sethian, Fronts propagating with curvature-dependent speed: Algorithms based on hamilton-jacobi formulations, J. Comput. Phys. **79**, 12 (1988).

[32] M. Sussman, P. Smereka, and S. Osher, A level set approach for computing solutions to incompressible two-phase flow, J. Comput. Phys. **114**, 146 (1994).

[33] C. Sun, E. Can, R. Dijkink, D. Lohse, and A. Prosperetti, Growth and collapse of a vapour bubble in a microtube: The role of thermal effects, J. Fluid Mech. **632**, 5 (2009).

[34] C. Pozrikidis, *Fluid Dynamics: Theory, Computation, and Numerical Simulation* (Springer, Berlin, 2009).

[35] See Supplemental Material at http://link.aps.org/supplemental/10.1103/PhysRevFluids.2.014301 for high-speed photography of cell deformation by a laser generated bubble in an axisymmetric confinement.

[36] S. Mochizuki and W.-J. Yang, Self-sustained radial oscillating flows between parallel disks, J. Fluid Mech. **154**, 377 (1985).

[37] T. Tandiono, D. S.-W. Ow, L. Driessen, C. S.-H. Chin, E. Klaseboer, A. B.-H. Choo, S.-W. Ohl, and C.-D. Ohl, Sonolysis of *Escherichia coli* and *Pichia pastoris* in microfluidics, Lab Chip **12**, 780 (2012).